

## Title

# Growth and Structure of alpha-Ta films for Quantum Circuit Integration

## Authors

Loren D. Alegria[1]\*, Eunjeong Kim[1], Soohyun Im[2], Alex Abelson[1], Paul M. Voyles[2], Jonathan L. Dubois[1], Yaniv J. Rosen[1]

## Affiliations

[1] Lawrence Livermore National Laboratory

[2] University of Wisconsin Madison

\*corresponding author: [alegria4@llnl.gov](mailto:alegria4@llnl.gov), 7000 East Ave. Livermore, CA 94550 USA

## Abstract

Tantalum films incorporated into superconducting circuits have empirically low surface losses, resulting in long-lived qubit states. Remaining loss pathways originate in microscopic defects which manifest as two level systems (TLS) at low temperature. Defects bound qubit performance, recommending careful consideration of tantalum film structures. Here we investigate the growth of tantalum on sapphire, Si, and photoresist substrates by magnetron sputtering. In the case of sapphire, we present procedures for growth of fully-oriented films with  $\alpha$ -Ta [1 1 1] //  $\text{Al}_2\text{O}_3$  [0 0 1] and  $\alpha$ -Ta [1 -1 0] //  $\text{Al}_2\text{O}_3$  [1 0 0] having residual resistivity ratios  $\sim 60$  for 220 nm thick films. On Si, we find a complex grain texturing with Ta [1 1 0] normal to the substrate and RRR  $\sim 30$ . We also demonstrate airbridge fabrication using Nb to nucleate  $\alpha$ -Ta on photoresist surfaces. Superconducting resonators patterned from films on sapphire show TLS-limited quality factors averaging  $1.6 \pm 0.4 \times 10^6$  at 10 mK. Structural characterization using scanning electron microscopy, X-ray diffraction, low temperature transport, secondary ion mass spectrometry, and transmission electron microscopy describe the dependence of residual impurities and screw dislocation density on processing conditions.

## Keywords:

Vapor phase epitaxy, Superconducting materials, Metals, Surface structure, Line defects, X-ray diffraction

## Introduction

Studies of two level systems (TLS) in superconducting qubit devices have sought the microscopic origins of qubit decoherence.<sup>1-3</sup> Although atomic displacements in junction oxides are the best understood TLS, recent work highlighting the role of surface oxides, hydrides and microfractures illustrates the complexity of the problem.<sup>4-6</sup> Overall, most posited decoherence sources argue for the development of superconductor films with high quality oxides and uniform crystal structure.

Recent demonstrations of high-performance qubits fabricated largely using Tantalum has drawn interest to materials science considerations particular to this superconductor.<sup>7,8</sup> The

apparent performance advantage over more conventional metals (such as Al and Nb) has been attributed to both the surface cleanliness enabled by tantalum's resistance to corrosive cleaning agents (e.g., piranha) and its favorable native oxides which exhibit low loss and magnetism.<sup>7-10</sup> The growth of superconducting Ta films with controlled microstructure is therefore of natural interest for the fabrication of qubits with minimal dissipation.

Substrate requirements for superconducting circuits include minimal piezoelectricity, low impurity concentrations, and suitable processing stability. Samples of heat-exchange-growth sapphire and float-zone silicon, as used here, have low-temperature loss tangents suitable for ms-scale qubit lifetimes.<sup>11-14</sup>

Ta has two distinct polymorphs. The body-centered-cubic  $\alpha$ -Ta has a bulk superconducting critical temperature,  $T_c = 4.4$  K, while  $\beta$ -Ta—a tetragonal  $\sigma$ -phase with  $T_c \sim 0.5$  K—is typically disordered but forms on many substrates at room temperature. Empirically, the  $\beta$  phase consistently exhibits much higher losses in the few-photon limit relevant to superconducting qubits, motivating our investigation of ordered  $\alpha$ -Ta films.<sup>15</sup>

Growth of Ta on sapphire structurally follows the model of Nb.<sup>15-19</sup> Sapphire permits epitaxial growth at the elevated temperatures required to stabilize the  $\alpha$ -phase.<sup>20</sup> Like Nb, coherent epitaxy of Ta can occur on the a- and c-plane of sapphire.<sup>17,21</sup> For 100 nm-scale film thicknesses as often used for circuits, the [110] Ta films that form on the a-plane show uniaxially elongated grain texture.<sup>22,23</sup> On the c-plane, Ta can grow in the [110] direction, in which regime the lattice mismatch leads to the formation of columnar grains which are elongated in the sapphire [100], [010], or [110] directions.<sup>7,24</sup> At higher temperatures or reduced background pressure, Ta grows in the [111] direction with a single azimuthal orientation,  $\alpha$ -Ta [1 -1 0] //  $\text{Al}_2\text{O}_3$  [100], equivalent to  $\alpha$ -Ta (-1 1 0) //  $\text{Al}_2\text{O}_3$  (2 -1 0).<sup>25</sup> The lattice mismatch between the trigonal interfacial lattices is 1.9 % as illustrated in Fig. 1 A.<sup>25-27</sup>

On the other hand, studies of growth on silicon surfaces have not seen crystallographic registry but  $\alpha$ -Ta grows at temperatures above approximately 300 °C as well as at very low temperatures ( $\sim 9$  K).<sup>24,28,29</sup> At low temperatures, the Si-Ta interphase is suppressed but the density of grain boundaries is high. Silicon's advantages in manufacturability may outweigh any negative impact of these dislocations on qubit performance.<sup>28</sup>

Finally, growth of superconducting Ta on organic surfaces is of interest for airbridge definition or for the creation of other free-standing structures. Airbridges allow superconducting circuits to overcome the severe topology constraints of planar circuits. Typically made from Ti or Al, airbridges are widely used to accurately define resonant modes and waveguides.<sup>30-32</sup> Although possibly less constrained than qubit materials, airbridges should have low loss, and ideally withstand the same surface treatments, such as piranha cleaning, as the base superconductor layer. This motivates fabrication of airbridges from superconducting Ta.

The three-dimensional structure of the airbridge can be defined with a range of template materials, but photoresist templates afford the most flexibility, and are particularly suitable for Ta, since it is compatible with piranha etchant, which removes highly cross-linked organic residues from the sputtering process. Below we demonstrate that a 2 nm layer of Nb suffices to phase-pure  $\alpha$ -Ta on a photoresist substrate, permitting superconducting Ta airbridges.

## Growth Studies

Table 1 presents Ta depositions on sapphire substrates, in which parameters were varied in order to minimize the film resistivity—a useful proxy for the density of scattering sites in the film and the presence of  $\beta$ -Ta. Sample Sph 0 was grown by Star Cryoelectronics Inc., whereas the others were deposited in-house. The clearest trend in this growth series is the effect of the chamber condition. The sample pairs Sph 4/5, Sph 6/7, Sph 8/9, and Sph 11/12 were each performed identically and immediately in sequence, and, in each case, the second deposit was appreciably more conductive. This indicates that with each successive deposition, the chamber environment becomes cleaner, leading to fewer scattering sites in the Ta. This observation is of considerable practical value, since one can judge the magnitude of effects due to growth conditions versus chamber condition. Following the MBE literature, we anticipated the highest quality films at the highest growth temperatures, but found increased resistivity at 800 °C, possibly due to chamber outgassing.<sup>20,33</sup> Although the chamber history effect makes precise optimization challenging, low DC sputtering power,  $P_{DC} < 150$  W and a temperature of 625 °C were suitable for highly conductive films, approaching the bulk resistivity (13.5  $\mu\Omega$ -cm).

ID	$T_A$ [°C]	$T_G$ [°C]	Nucl.	$P_{DC}$ [W]	$\rho$ [ $\mu\Omega$ -cm]	$R_{300K}/R_{5K}$	XRD	$\delta_{110}$ (deg.)
Sph 0*	-	500	no	-	23	7.8	$\alpha$ -110	0.21
Sph 1	25	25	yes	270	27.3	2.6	$\alpha$ -110	0.28
Sph 2	25	25	yes	270	27.7	-	-	-
Sph 3	650	625	yes	150	16.2	-	-	-
Sph 4	825	800	no	150	16.9	-	-	$\delta_{111} = 0.24$
Sph 5	825	800	no	150	16.1	-	-	-
Sph 6	650	625	no	270	18.3	-	-	-
Sph 7	650	625	no	270	16.1	-	-	-
Sph 8	650	625	no	150	15.9	-	-	-
Sph 9	650	625	no	150	15.2	-	-	-
Sph 10	650	625	no	75	14.4	62	$\alpha$ -111	$\delta_{111} = 0.22$
Sph 11	650	625	no	40	14.5	-	-	-
Sph 12	650	625	no	40	14.4	-	-	-

**Table 1. Tantalum films on c-plane sapphire.** For a given wafer,  $T_A$  is the *in situ* annealing temperature held for three minutes prior to growth,  $T_G$  is the growth temperature, *Nucl.* indicates the use of a 2 nm Nb nucleation layer,  $P_{DC}$  is the DC power applied to the 3 inch target,  $\rho$  is the room temperature resistivity, XRD is the phase and orientation indicated by XRD, and  $\delta_{110}$  is the width of the (110) reflection in XRD. Room temperature resistivity was strongly indicative of phase and defect density. Of the parameters varied, the batch index had the clearest impact on resistivity: in sequential, nominally identical growths the second consistently showed lower resistivity (compare Sph 4/5, Sph 6/7, Sph 11/12), indicating that background impurities impact defect density in the films. \*Sph 0 was deposited by a commercial vendor and is 200 nm in thickness. All other samples are 220 nm in thickness.

Next, Table 2 presents illustrative growths performed on Si. Samples Si 1 and Si 2 had very high resistivity, indicating  $\beta$ -Ta formation at the low growth temperatures, independent of whether the wafer was annealed *in situ*. Comparing Si 3 and Si 4, nucleation at moderately elevated temperatures increases crystallinity as compared to nucleation at room temperature. At higher temperatures (Si 5 and 6), a more crystalline film forms. Comparing Si 5 and Si 6, the film product is entirely independent of Si orientation, with identical resistivity ratios in films on (110)- and (100)-Si (cf. Fig 4 B) suggesting that the interfacial layer fully buffers the Si lattice.

ID	Orient.	T <sub>A</sub> [°C]	T <sub>G</sub> [°C]	Nucl.	P <sub>DC</sub> [W]	$\rho$ [ $\mu\Omega$ -cm]	R <sub>300 K</sub> /R <sub>5 K</sub>	XRD	$\delta_{110}$ (deg.)
Si 1	(100)	25	400	no	270	290	-	$\alpha, \beta$	0.42
Si 2	(100)	650	300	no	150	180	-	-	-
Si 3	(100)	25	25	yes	270	34.8	-	$\alpha$ -110	0.40
Si 4	(100)	650	300	yes	150	19.3	-	-	-
Si 5	(100)	650	625	no	75	15.9	32	$\alpha$ -110	0.23
Si 6	(110)	650	625	no	75	15.7	32	$\alpha$ -110	0.24
Resist	-	25	25	yes	270	29	-	$\alpha$ -110	0.52

**Table 2. Tantalum films on silicon and resist substrates.** At lower temperatures (Si 1 - 4) a Nb nucleation layer proved necessary for  $\alpha$ -phase growth, independent of annealing. At high temperature, the film structure was independent of silicon orientation. Notation as in Table 1.

Comparing the films on Si and Sapphire, the room temperature resistivity is a reliable indicator of  $\alpha/\beta$  phase, as others observed,<sup>18</sup> but not a definitive indicator of crystal orientation. Si 5/6 and Sph 5 have nearly identical resistivities, but XRD indicate that Si 5/6 had [110] orientation while Sph 5 had [111]. Ta crystallization is known to be sensitive to background impurities,<sup>25</sup> yet even in the general-purpose sputtering system employed here, proper chamber conditioning and straightforward variation of growth parameters result in films with high conductivity, a critical heuristic for the phase.

### Structural and Chemical Characterization

Depending on substrate and deposition conditions, magnetron-sputtered  $\alpha$ -Ta films exhibit a wide variety of surface structures.<sup>34</sup> Fig. 1 serves to illustrate this morphological variety.

Fig. 1 A shows the alignment between the  $\alpha$ -Ta (111) and Al<sub>2</sub>O<sub>3</sub> (001) surfaces as typically occurs at higher growth temperatures.<sup>25</sup> Such growth temperatures were employed for Samples Sph 3-12. Fig. 1 B and C show high-angle annular dark-field transmission electron microscopy (HAADF-STEM) images and scanning electron microscopy (SEM) images of films grown under these conditions (Sph 10 and Sph 8, respectively). In TEM, a very sharp interface between the Ta and sapphire is observed and grain boundaries are not apparent. On the other hand, SEM showed

characteristic point-like defects in all such surfaces (as in Fig 1 C). The appearance of these is consistent with ubiquitously-observed screw dislocations in bcc metals. Typically possessing  $\frac{1}{2}[111]$  Burgers vectors, these one dimensional defects appear as points or small triangles where they intersect the surface.<sup>35,36</sup> By contrast, Fig. 1 D shows an SEM image of a  $[110]$ -oriented Ta film (Sph 0) with clear grain boundaries.<sup>24</sup> In this way, the SEM morphology of freshly prepared films can be used to assess the film orientation.

On Si, a more complex grain structure appears. At low growth temperature, grains have truly random azimuthal orientation,<sup>24</sup> but at elevated growth temperature longer range ordering effects are apparent. Fig. 1 E shows an SEM image of Si 5, and the emergence of an in-plane texture featuring alternating bands of wide and narrow grains. Si 6 showed an effectively identical texture. The SEM signal contrast here was visible at high ( $\sim 20$  kV) beam acceleration, and thus derives from proportionately deep within the film, rather than describing surface topography. Cross-sectional TEM imaging (Fig S3 A) confirmed the surface to be smooth with occasional grain boundaries. These findings are consistent with others' that Ta forms at random in-plane rotations at the scale accessible by XRD,<sup>28</sup> but the aligned bands we observe indicate ordering of the Ta at up to 100  $\mu\text{m}$  scales (c.f. Fig. S3 B). Given the similarity of this length scale to that of qubit lithography, it is possible that the intersection of such bands with qubit electrodes could influence the predictability of qubit quality.

Fig. 1 F shows an SEM image of the foot of an airbridge grown by nucleation on a photoresist template. The top of the image is the contact region, which grew on the sapphire, and the bottom of the image is the suspended film, which grew on the photoresist. In contrast to growth on cleaner sapphire surfaces, the contact crystallites are randomly oriented due to residues from the lithography and oxygen-plasma cleaning steps that create the scaffold. The contacts show a coarser grain structure than in the bridge span and both show faceting, which is absent in  $\beta$ -Ta films, indicating the  $\alpha$ -phase.<sup>24</sup> The phase apparent from SEM was confirmed by XRD and transport as described subsequently.

Fig. 2 shows the procedure for airbridge fabrication. First, a template structure on sapphire is formed using two AZ1518 photoresist layers. The first layer of resist is spun to a thickness of 2 microns, baked at 90 °C and patterned into rectangles defining the 'scaffold' of the bridge (Fig. 2 A). The sample is then heated ('reflowed') at 140 °C for five minutes to round the scaffold (Fig. 2 B). Next, another 2 micron layer of AZ1518 is spun and patterned to form the rectangular windows defining the perimeter of the bridge. The final template structure is shown in the optical image in Fig. 2 C.

The Ta deposition on this photoresist template is identical to the process described in Ref. <sup>24</sup>: 2 nm of Nb is sputtered at ambient temperature, followed by 200 nm of Ta. The wafer is then soaked in acetone, removing the metal that was not within the airbridge perimeter (liftoff). After rinsing in isopropanol and drying with nitrogen, the airbridges are as shown in Fig. 2 D-E. Fig. 2 D is an SEM image captured at an angle to show that the scaffold is fully removed. [For perspective, the bridges shown in Fig. 2 D are the ones created by the masks in the dashed area of Fig. 2 C.] Fig. 2 E is an optical microscope image which shows a stubborn residue around the perimeter of the scaffold. These particular bridges shared a common scaffold, so the residue forms lines joining the four bridges. Finally, this wafer was immersed in a fuming Piranha bath (3 parts of concentrated

sulfuric acid and 1 part 30 wt. % hydrogen peroxide) for 1 hour. It was then rinsed in deionized water and ultrasonically cleaned for 1 minute in isopropanol. After this cleaning step the organic residues were completely removed as seen in Fig. 2 F.

We directly characterized the phase of the suspended bridges by carefully considering the contributions of suspended and non-suspended regions to the overall resistance of a contacted bridge (such as in Fig. 2 G). By performing four-terminal resistance measurements of control strips with no bridges and comparing these to bridges, we determined the bridges to have a resistivity of  $29 \pm 1 \mu\Omega\text{-cm}$ . Purely  $\beta$ -phase films would have a resistivity approximately an order of magnitude higher, and films with similar resistivity (e.g. Si 3) have  $T_c = 4.1$  K. In addition, XRD of films grown in the same way but on a uniform,  $2 \mu\text{m}$  thick,  $90^\circ\text{C}$ -baked AZ1518 photoresist layer show no detectable  $\beta$  fraction (see Fig. 3).

Fig. 3 shows a comparison of  $\theta$ - $2\theta$  XRD spectra of several Ta films. The [110]-oriented films on sapphire (Sph 0, 1) show a set of peaks between  $30$  and  $35$  which we ascribe to strain around grain boundaries.<sup>7,24</sup> On the other hand,  $\alpha$ -Ta films on silicon (Si 1,3,5,6) show no such extra peaks, only the (110) reflection ( $2\theta = 38.5^\circ$ ). Growth at insufficiently high temperature on Si (Sample Si 1) shows a clear  $\beta$ -[002] peak as well ( $2\theta = 33.7^\circ$ ). The [111]-oriented Sph 10 and 4 films show a single reflection in the [222] direction ( $2\theta = 107.8^\circ$ ) with no contribution from [110] or the minor peaks. The Ta film nucleated on photoresist, labeled '*Resist*,' shows no  $\beta$  or  $\alpha$ -[111] component.

The quality of the films grown on sapphire at high temperature was borne out in variable temperature resistance measurements. The film Sph 10 showed  $T_c$  close to the bulk value and residual resistivity ratio,  $\text{RRR} = 62$ , almost double that of the films grown on Si under the same conditions (c.f. <sup>37</sup>), and almost 10 times that of [110] films on sapphire. The RRR provides a sensitive measure of the defect density.

The lower  $T_c$  and RRR of the films on Si may be compared to the TEM data of Fig. S1. Here an 8-10 nm boundary layer is apparent between the Si and Ta. TEM-based EDS indicated the boundary layer to smoothly interpolate between pure Si and Ta (to within the  $\sim 1\%$ ), and scattering within the disordered region might explain the lower RRR. Nonetheless, the RRR in the films on Si was much higher than in the fine-grained, nucleated films (such as Sph 3 in Fig. S1A).

Although TEM shows the Ta films grown at high and low temperatures to have clear crystalline phases, Secondary Ion Mass Spectroscopy (SIMS) reveals a substantial quantity of contaminants in the films, as shown in Fig. 5. All the films grown at room temperature had a rougher surface ( $\sim 10$  nm in roughness) than the films grown at  $625^\circ\text{C}$ . The SIMS data represents a convolution of this roughness (and roughness developed during the SIMS erosion process) with the actual local concentration. Even considering this, H, C, and O appear much further beneath the surface of the room-temperature-grown film than the higher temperature-grown film (c.f. Fig 6 A and B). Percolation of light elements along grain boundaries and the volatility of many C, H, and O-bearing species at the higher temperature may explain this data. In the case of Sph 10 (Fig. 5 C), the  $10^{19} \text{ cm}^{-3}$  scale of impurities in the film interior is not far from the nominal impurity concentration of the 99.9 % Ta sputtering target.

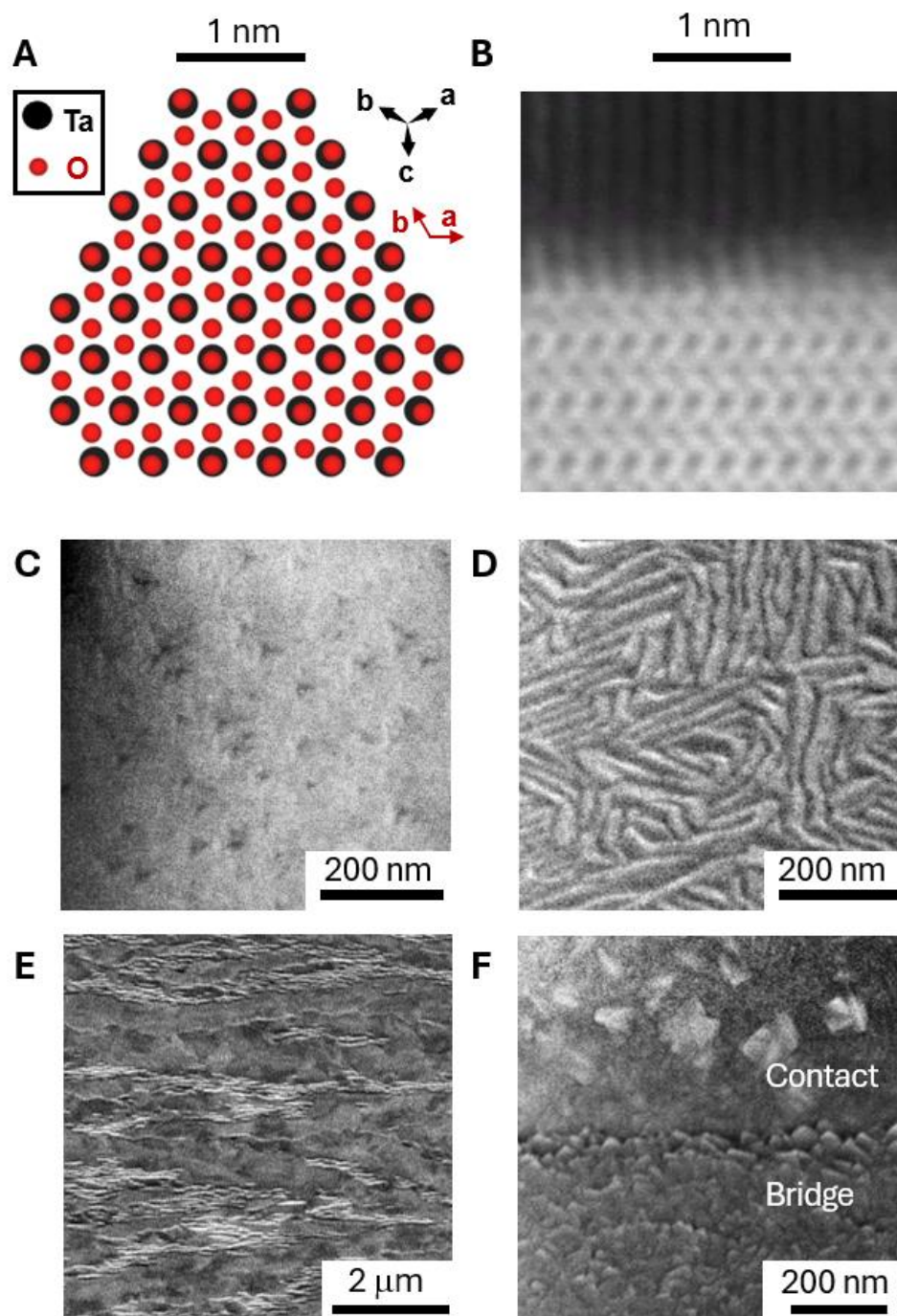
This same film, Sph 10, was patterned into hanger-mode, frequency-multiplexed coplanar waveguide  $\lambda/4$  resonators, using the mask design of Ref. <sup>38</sup> The resonators were defined with an SF<sub>6</sub> etch and then cleaned with piranha and buffered oxide etch before being measured using a vector network analyzer in a dilution refrigerator at 10 mK.

Fig. 6 summarizes the results of these resonator measurements. Although there were two resonators on the chip with very low quality factors, the six resonators analyzed (using the model of Ref. <sup>39</sup>) had an average TLS-limited internal quality factor  $Q_i = 1.6 \pm 0.4 \times 10^6$  as derived from the fitted curves shown in the figure. The dispersity of the resonators of Fig. 6 illustrates the susceptibility of such measurements to inhomogeneities that develop during microfabrication, but the overall high quality factor indicates that such films are suitable as the primary superconducting layer within present high-performance qubit circuits.<sup>11</sup>

### **Concluding Remarks**

We have demonstrated suitable growth conditions for Ta films with low densities of scattering defects on technologically important substrates, including very ordered films on sapphire. These may bear upon any of the diverse microfabrication applications of Ta films.<sup>40</sup> For superconducting qubits, the demonstration of growth on polymer substrates allows for piranha-compatible bridges.<sup>41,42</sup> In these suspended structures, the nature of the film underside is of continued interest, and loss in this surface may be tied to effective removal of the nucleating species.<sup>43</sup>

On Si diffusion uniformly depresses the stability of the superconducting state, encouraging the exploration of low-loss diffusion barriers, and innovative approaches to low temperature crystalline growth. Continued improvements of solid state qubits overall will require simultaneous optimization of strain distribution and qubit geometry.<sup>44</sup>



**Figure 1. Characteristic microstructures of  $\alpha$ -Ta grown on sapphire, Si, and photoresist.** (A) The (001) sapphire oxygen bulk loci approximately match the (111) Ta surface. (B) In [111]-oriented Ta films, a sharp interface is observed in HAADF-STEM imaging. (C) As seen in SEM, the [111]-Ta film on sapphire shows a sparse array of screw dislocations. (D) By contrast, a [110]-Ta film on sapphire shows distinct grain boundaries. (E) On silicon, Ta films grown at 650 °C show a banded grain texture. (F) An SEM image of the base of a Nb-nucleated Ta airbridge, showing crystallites of the contact region (top part of image) and bridge region (bottom part of image). (B-E Samples Sph 10, Sph 8, Sph 0, Si 5 respectively).



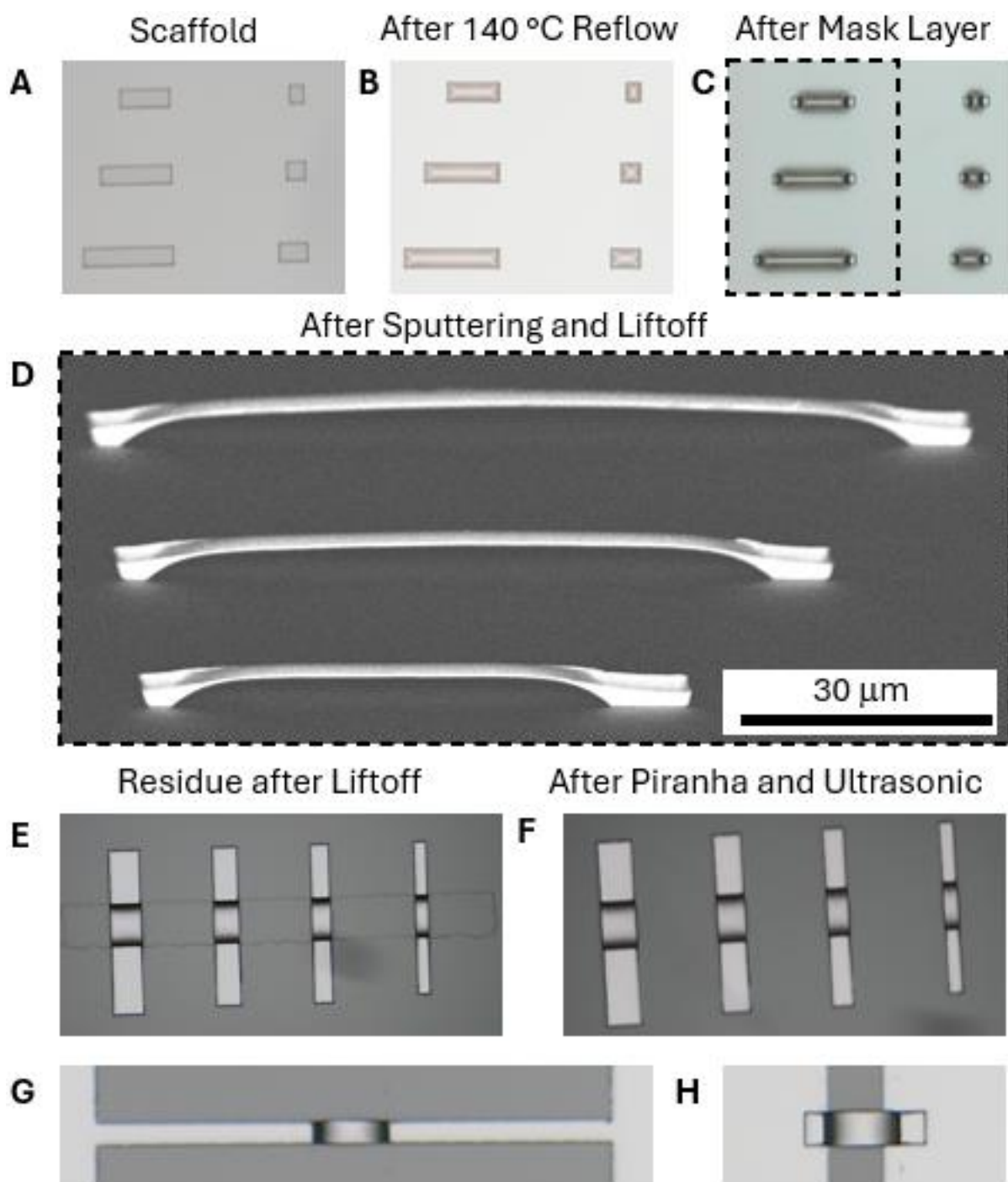


**Figure 2. Growth of  $\alpha$ -Ta on photoresist enables airbridge definition.** (A) A template for liftoff of airbridges is defined by (B) heating a patterned photoresist layer to form a smooth slope on the perimeter of the ‘scaffold’ and then (C) patterning a second ‘mask’ layer on top to define the perimeter of the bridge and contacts. (D) A tilted SEM image of bridge structures after Nb/Ta sputtering and acetone liftoff, showing that the scaffold is fully removed. (E-F) A residue around the scaffold perimeter after liftoff is readily removed by piranha etching. (G-H) Devices for transport measurement. (All images are optical apart from D.)

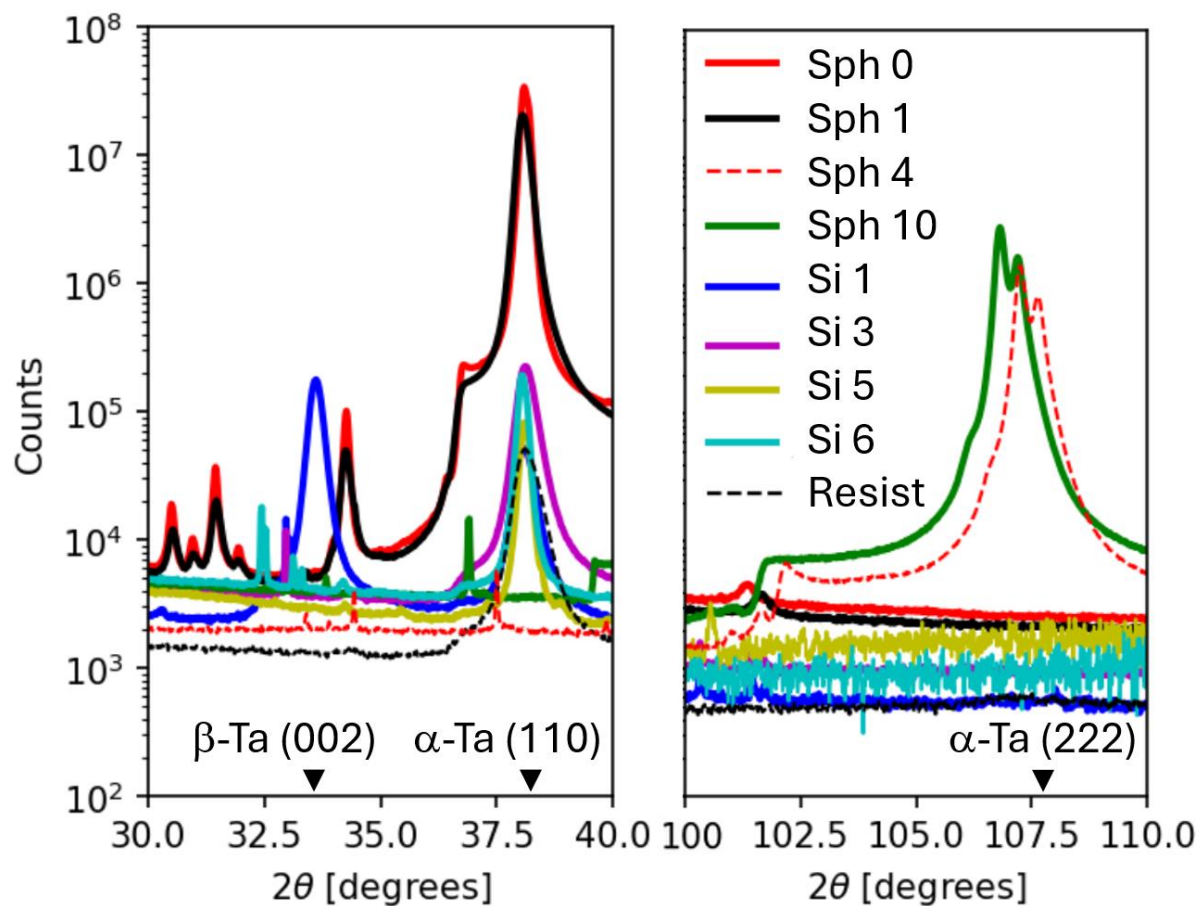


**Figure 3. X-ray diffraction ( $\theta$ - $2\theta$  with continuous  $\phi$  rotation) of Ta films grown on sapphire, silicon, and AZ1518 photoresist.** [111]-oriented Ta (Sph 10, Sph 4) shows the sharpest reflections and almost no features in the region characteristic of [110]-oriented films (Sph 0,1 and Si 3-6), and conversely none of the other films show a (111) reflection.

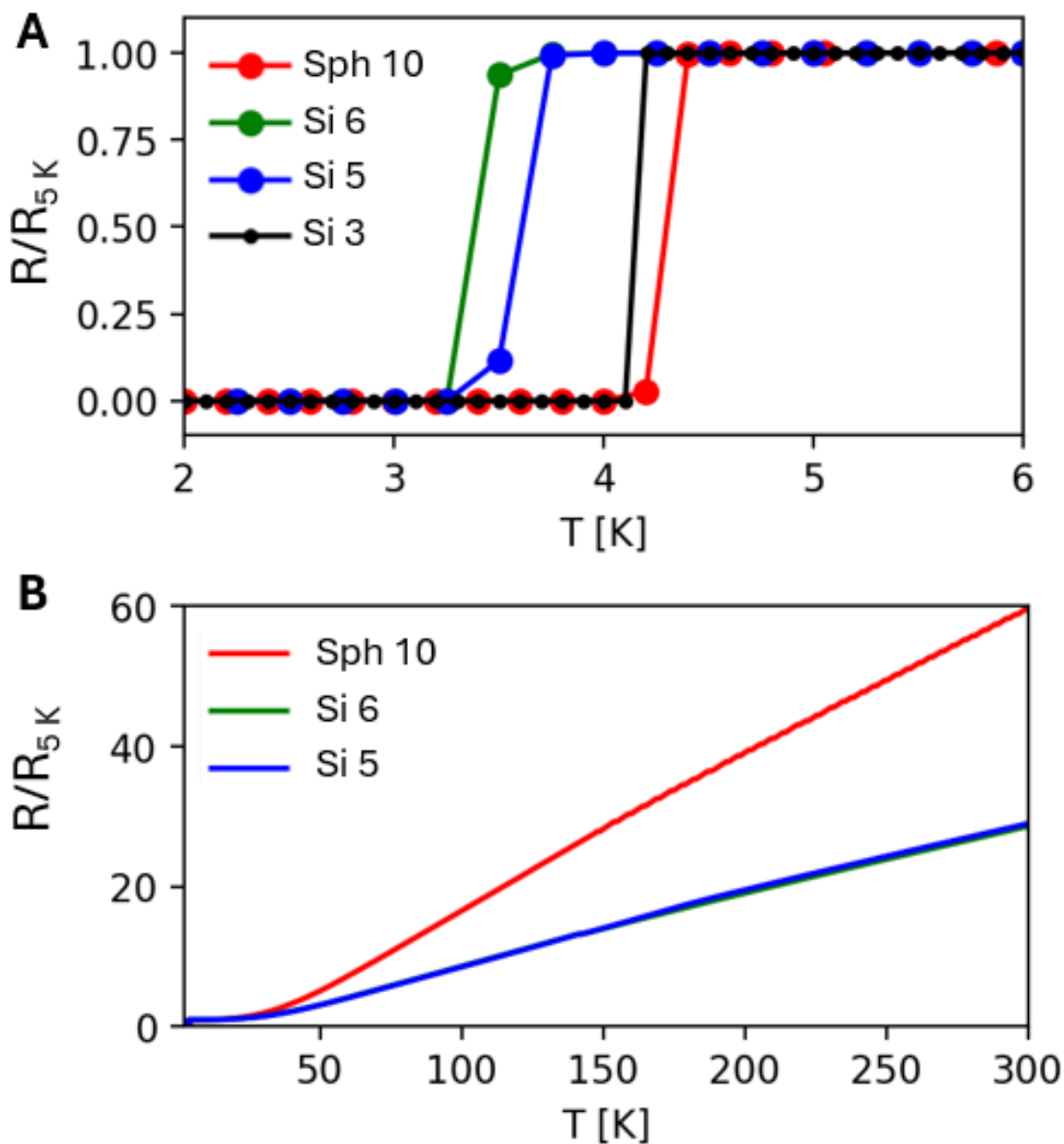


**Figure 4. Variable-temperature transport measurements.** DC Resistance measurements show (A) the highest critical temperatures to be reached by Ta films grown at high temperature on sapphire (Sph 10), room-temperature-nucleated Ta to have a slightly diminished  $T_c$  (Si 3) and films grown under the same high temperature conditions but on Si to have a lower  $T_c$  and (B) resistivity ratio (Si 5, 6).

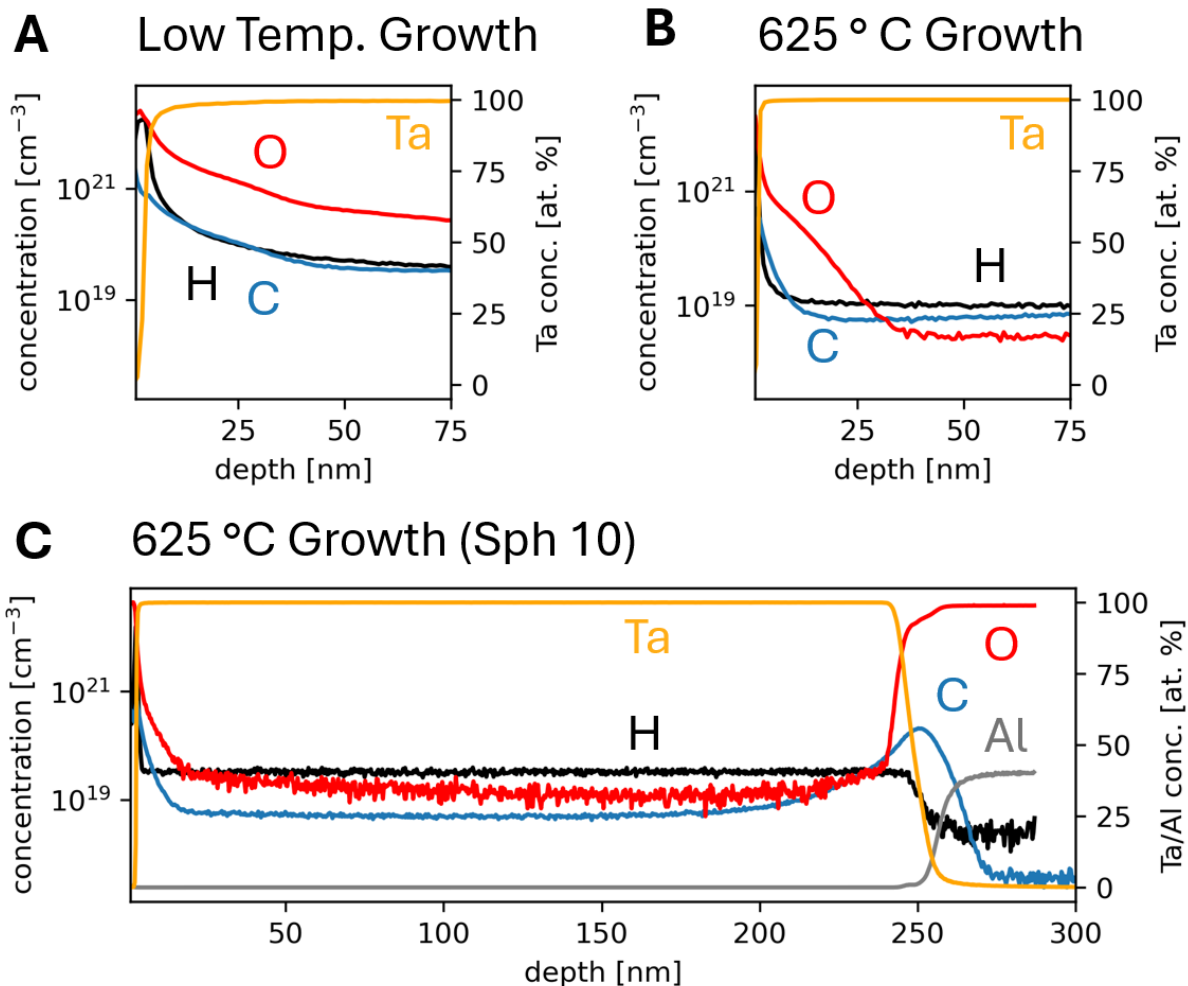


**Figure 5. Secondary ion mass spectroscopy (SIMS) of films grown at high and low temperatures.** (A) SIMS of the surface of a film nucleated at room temperature showing H, C and O contaminants to extend further into the film surface as compared to a film (B) grown at high temperature (this film was grown under conditions similar to films Sph 6-12). (C) In Sph 10, which showed a high residual resistivity ratio and resonator internal quality factors, there remain substantial quantities of H, C, and O as compared to the sapphire substrate.

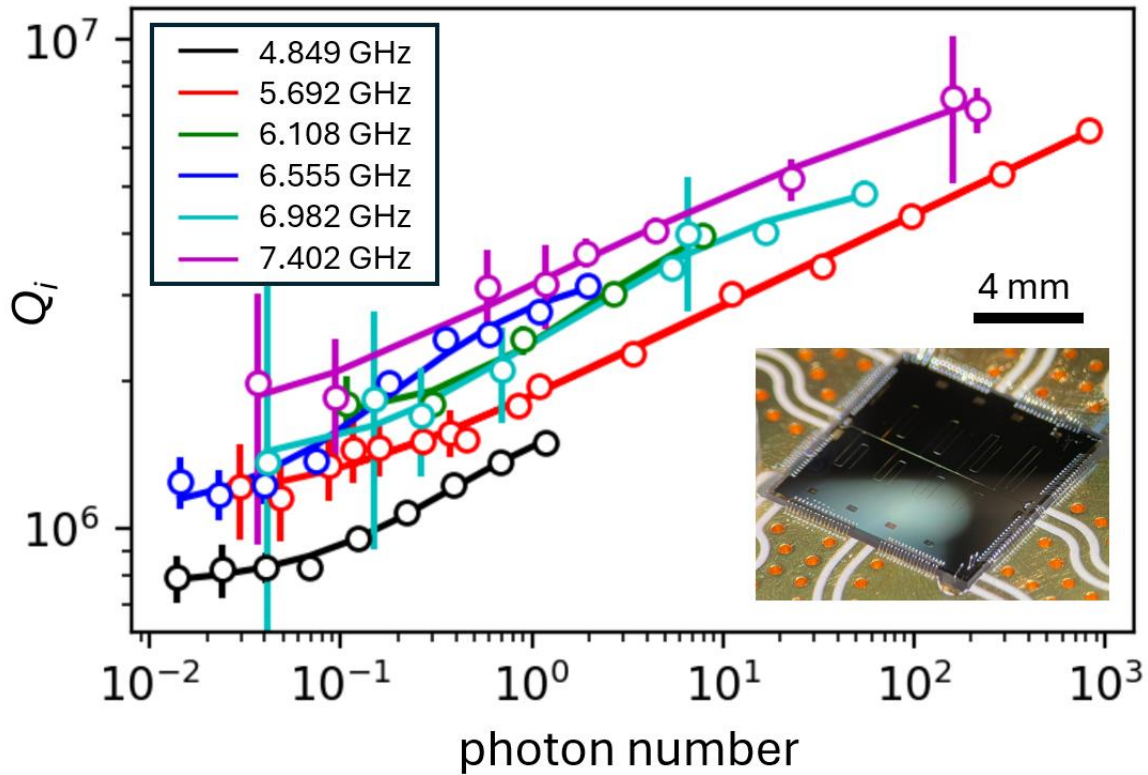


**Figure 6. Resonator Measurements.** Internal quality factor  $Q_i$  of coplanar waveguide resonators patterned from Sample Sph 10, measured at 10 mK. The legend specifies the resonator center frequencies at high power. The center conductor width of these six resonators is  $6\ \mu\text{m}$  and the gap is  $3\ \mu\text{m}$ .<sup>38</sup> The error bars represent the uncertainty in the internal quality factor fit parameter. Inset, photograph of the resonator die.

### Acknowledgements

This material is based upon work supported by LLNL-LDRD-24-ER-045, (supporting contributions by J.L.D. and E. K.); by AFRSO MQC (supporting the contributions of L.D.A. and A. A.); and by U.S. Department of Energy, Office of Science, Basic Energy Sciences, under award number DE-SC0020313 (supporting the contributions of S.I. P.V.). This work was performed in part under the auspices of the U.S. Department of Energy by Lawrence Livermore National Laboratory under contract DE-AC52-07NA27344. Lawrence Livermore National Security, LLC.

### Author Contributions

**L.D.A.:** Conceptualization, Investigation, Data curation, Formal analysis, Writing - original draft, Supervision. **E.K.:** Investigation (XRD,PPMS). **S.I.:** Investigation (TEM). **A.A.:** Investigation (XRD, PVD), Methodology, Writing - review & editing. **P.M.V.:** Supervision, Writing - review & editing. **J.L.D.:** Conceptualization, Supervision. **Y.J.R.:** Formal analysis.

### Data Statement

The data contributing to the conclusions of this work are available from the authors upon reasonable request.

## References

- 1 Kristen, M. *et al.* Observation of giant two-level systems in a granular superconductor. *arXiv preprint arXiv:2307.09078* (2023).
- 2 Bilmes, A., Volosheniuk, S., Ustinov, A. V. & Lisenfeld, J. Probing defect densities at the edges and inside Josephson junctions of superconducting qubits. *npj Quantum Information* **8**, 24 (2022). <https://doi.org/10.1038/s41534-022-00532-4>
- 3 Rosen, Y. J., Khalil, M. S., Burin, A. L. & Osborn, K. D. Random-defect laser: Manipulating lossy two-level systems to produce a circuit with coherent gain. *Physical review letters* **116**, 163601 (2016).
- 4 Phillips, W. A. Two-level states in glasses. *Reports on Progress in Physics* **50**, 1657-1657 (1987). <https://doi.org/10.1088/0034-4885/50/12/003>
- 5 Anthony-Petersen, R. *et al.* A stress induced source of phonon bursts and quasiparticle poisoning. *arXiv preprint arXiv:2208.02790* (2022).
- 6 Chayanun, L. *et al.* Characterization of process-related interfacial dielectric loss in aluminum-on-silicon by resonator microwave measurements, materials analysis, and imaging. *arXiv preprint arXiv:2403.00723* (2024).
- 7 Place, A. P. M. *et al.* New material platform for superconducting transmon qubits with coherence times exceeding 0.3 milliseconds. *Nature Communications* **2021 12:1** **12**, 1-6 (2021). <https://doi.org/10.1038/s41467-021-22030-5>
- 8 Wang, C. *et al.* Towards practical quantum computers: transmon qubit with a lifetime approaching 0.5 milliseconds. *npj Quantum Information* **2022 8:1** **8**, 1-6 (2022). <https://doi.org/10.1038/s41534-021-00510-2>
- 9 Crowley, K. D. *et al.* Disentangling Losses in Tantalum Superconducting Circuits. (2023). <https://doi.org/10.48550/ARXIV.2301.07848>
- 10 Mozara, R. *et al.* Atomically thin oxide layer on the elemental superconductor Ta(001) surface. *Physical Review Materials* **3**, 094801 (2019). <https://doi.org/10.1103/PhysRevMaterials.3.094801>
- 11 McRae, C. R. H. *et al.* Materials loss measurements using superconducting microwave resonators. *Review of Scientific Instruments* **91**, 091101-091101 (2020). <https://doi.org/10.1063/5.0017378>
- 12 Ganjam, S. *et al.* Surpassing millisecond coherence in on chip superconducting quantum memories by optimizing materials and circuit design. *Nat Commun* **15**, 3682 (2024). <https://doi.org/10.1038/s41467-024-47857-6>
- 13 Read, A. P. *et al.* Precision measurement of the microwave dielectric loss of sapphire in the quantum regime with parts-per-billion sensitivity. *Physical Review Applied* **19**, 034064 (2023).
- 14 Checchin, M., Frolov, D., Lunin, A., Grassellino, A. & Romanenko, A. Measurement of the Low-Temperature Loss Tangent of High-Resistivity Silicon Using a High- $Q$  Superconducting Resonator. *Physical Review Applied* **18**, 034013 (2022). <https://doi.org/10.1103/PhysRevApplied.18.034013>
- 15 Urade, Y. *et al.* Microwave characterization of tantalum superconducting resonators on silicon substrate with niobium buffer layer. *APL Materials* **12** (2024). <https://doi.org/10.1063/5.0165137>



- 16 Wagner, T., Lorenz, M. & Rühle, M. Thermal stability of Nb thin films on sapphire. *Journal of Materials Research* **11**, 1255-1264 (1996). <https://doi.org/10.1557/JMR.1996.0160>
- 17 Wildes, A. R., Mayer, J. & Theis-Bröhl, K. The growth and structure of epitaxial niobium on sapphire. *Thin Solid Films* **401**, 7-34 (2001). [https://doi.org/10.1016/S0040-6090\(01\)01631-5](https://doi.org/10.1016/S0040-6090(01)01631-5)
- 18 Colin, J. J., Abadias, G., Michel, A. & Jaouen, C. On the origin of the metastable  $\beta$ -Ta phase stabilization in tantalum sputtered thin films. *Acta Materialia* **126**, 481-493 (2017). <https://doi.org/10.1016/j.ACTAMAT.2016.12.030>
- 19 Lamelas, F. J., He, H. & Clarke, R. X-ray diffraction study of epitaxial Nb-Ta overlayers on sapphire. *Physical Review B* **38**, 6334-6334 (1988). <https://doi.org/10.1103/PhysRevB.38.6334>
- 20 Durbin, S. M., Cunningham, J. E. & Flynn, C. P. Crystal Direction Dependence of Interfacial Mixing in Nb-Ta Superlattices. *J Phys F Met Phys* **17**, L59-L63 (1987). <https://doi.org/10.1088/0305-4608/17/4/003>
- 21 Welander, P. B. & Eckstein, J. N. Strained single-crystal Al<sub>2</sub>O<sub>3</sub> grown layer by layer on Nb (110) thin films. *Applied physics letters* **90** (2007). <https://doi.org/10.1063/1.2747675>
- 22 Dhundhwal, R. et al. Tantalum thin films on a-plane sapphire for low-loss superconducting circuits. *Bulletin of the American Physical Society* (2024).
- 23 Jia, H. et al.  $\alpha$ -tantalum (110) films grown on a-plane sapphire substrate by molecular beam epitaxy for low-loss superconducting coplanar waveguide resonators. *arXiv preprint arXiv:2306.09566* (2023).
- 24 Alegria, L. D. et al. Two-level systems in nucleated and non-nucleated epitaxial  $\alpha$ -tantalum films. *Applied Physics Letters* **123** (2023). <https://doi.org/10.1063/5.0157654>
- 25 Gnanarajan, S., Lam, S. K. H. & Bendavid, A. Coexistence of epitaxial Ta(111) and Ta(110) oriented magnetron sputtered thin film on c-cut sapphire. *Journal of Vacuum Science & Technology A: Vacuum, Surfaces, and Films* **28**, 175-175 (2010). <https://doi.org/10.1116/1.3276801>
- 26 Pillet, S. et al. Recovering experimental and theoretical electron densities in corundum using the multipolar model: IUCr multipole refinement project. *Acta Crystallographica Section A: Foundations of Crystallography* **57**, 290-303 (2001). <https://doi.org/10.1107/S0108767300018626>
- 27 Mueller, M. H. The lattice parameter of tantalum. *Scripta Metallurgica* **11**, 693 (1977). [https://doi.org/10.1016/0036-9748\(77\)90141-7](https://doi.org/10.1016/0036-9748(77)90141-7)
- 28 Lozano, D. P. et al. Manufacturing high-Q superconducting  $\alpha$ -tantalum resonators on silicon wafers. (2022). <https://doi.org/10.48550/arxiv.2211.16437>
- 29 Palmstrom, C. et al. Low-Temperature MBE growth of superconducting Ta films on Silicon and Sapphire substrates. *Bulletin of the American Physical Society* (2024).
- 30 Chen, Z. et al. Fabrication and characterization of aluminum airbridges for superconducting microwave circuits. *Applied Physics Letters* **104** (2014). <https://doi.org/10.1063/1.4863745>
- 31 Marxer, F. et al. Long-Distance Transmon Coupler with cz-Gate Fidelity above  $99.8\%$ . *PRX Quantum* **4**, 010314 (2023). <https://doi.org/10.1103/PRXQuantum.4.010314>
- 32 Weides, M. et al. Phase qubits fabricated with trilayer junctions. *Superconductor Science and Technology* **24**, 055005 (2011). <https://doi.org/10.1088/0953-2048/24/5/055005>
- 33 Drimmer, M. et al. The effect of niobium thin film structure on losses in superconducting circuits. *arXiv preprint arXiv:2403.12164* (2024).
- 34 Torres-Castanedo, C. G. et al. Formation and Microwave Losses of Hydrides in Superconducting Niobium Thin Films Resulting from Fluoride Chemical Processing.

*Advanced Functional Materials* **n/a**, 2401365

[https://doi.org:https://doi.org/10.1002/adfm.202401365](https://doi.org/https://doi.org/10.1002/adfm.202401365)

- 35 Caillard, D. Geometry and kinetics of glide of screw dislocations in tungsten between 95K and 573K. *Acta Materialia* **161**, 21-34 (2018). [https://doi.org:10.1016/j.actamat.2018.09.009](https://doi.org/10.1016/j.actamat.2018.09.009)
- 36 Biener, M. M., Biener, J., Hodge, A. M. & Hamza, A. V. Dislocation nucleation in bcc Ta single crystals studied by nanoindentation. *Physical Review B* **76**, 165422 (2007).  
[https://doi.org:10.1103/PhysRevB.76.165422](https://doi.org/10.1103/PhysRevB.76.165422)
- 37 Shi, L. *et al.* Tantalum microwave resonators with ultra-high intrinsic quality factors. *Applied Physics Letters* **121** (2022). [https://doi.org:10.1063/5.0124821](https://doi.org/10.1063/5.0124821)
- 38 Kopas, C. J. *et al.* Simple coplanar waveguide resonator mask targeting metal-substrate interface. *arXiv preprint arXiv:2204.07202* (2022).
- 39 Khalil, M. S., Stoutimore, M. J. A., Wellstood, F. C. & Osborn, K. D. An analysis method for asymmetric resonator transmission applied to superconducting devices. *Journal of Applied Physics* **111**, 054510-054510 (2012). [https://doi.org:10.1063/1.3692073](https://doi.org/10.1063/1.3692073)
- 40 Westwood, W. D., Waterhouse, N. & Wilcox, P. S. *Tantalum Thin Films*. (Academic Press, 1975).
- 41 Alegria, L. *et al.* Growth of ordered Tantalum films and Integration into Quantum Circuits. *Bulletin of the American Physical Society* (2024).
- 42 Bu, K. *et al.* Tantalum airbridges for scalable superconducting quantum processors. *arXiv preprint arXiv:2401.03537* (2024).
- 43 Kotler, S. *et al.* Direct observation of deterministic macroscopic entanglement. *Science* **372**, 622-625 (2021).
- 44 Oh, S. *et al.* Elimination of two level fluctuators in superconducting quantum bits by an epitaxial tunnel barrier. *Physical Review B* **74**, 100502 (2006).  
[https://doi.org:10.1103/PhysRevB.74.100502](https://doi.org/10.1103/PhysRevB.74.100502)



## Supplementary Information: Growth and Structure of $\alpha$ -Ta films for Quantum Circuit Integration

Loren D. Alegria[1]\*, Eunjeong Kim[1], Soohyun Im[2], Alex Abelson[1], Paul M. Voyles[2], Jonathan L. Dubois[1], Yaniv J. Rosen[1]

[1] Lawrence Livermore National Laboratory

[2] University of Wisconsin Madison

\*corresponding author: alegria4@llnl.gov, 7000 East Ave. Livermore, CA 94550 USA

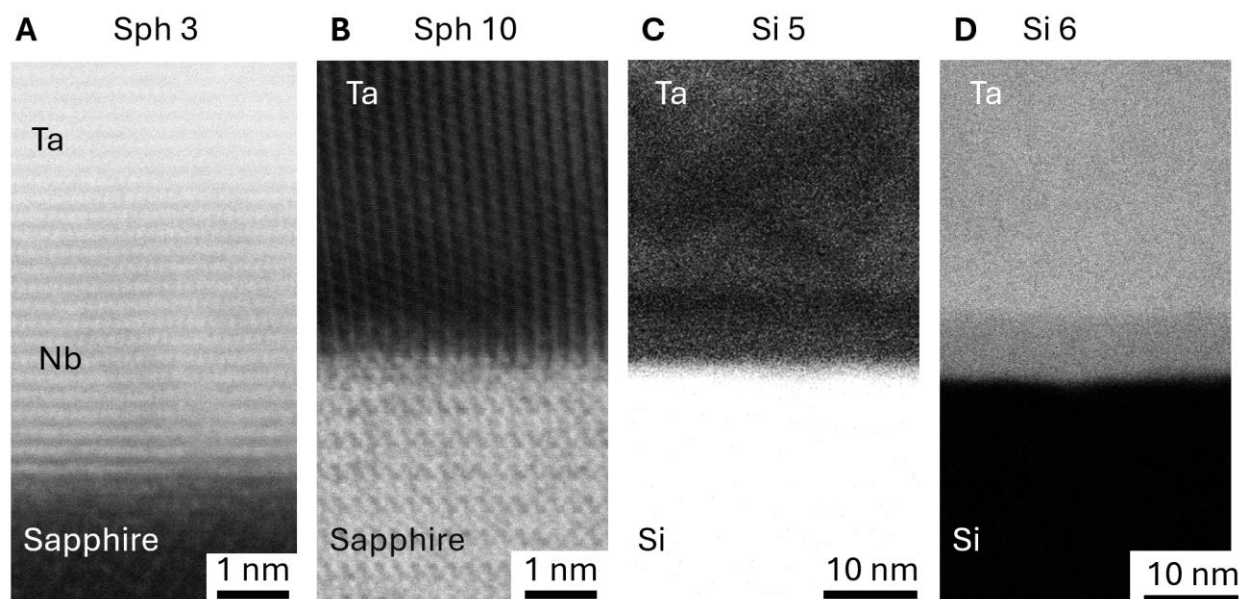


**Figure S1. Cross-sectional TEM Studies of  $\alpha$ -Ta films on Si and Sapphire.** (A) Films nucleated by Nb at room-temperature as described in the text show sharp interface to the sapphire, a clear Nb boundary layer and continuous epitaxy through the Nb-Ta interface. (B) In films grown at high temperature, there remains an atomically sharp interface to the sapphire. On (100) and (110) Si (C and D, respectively) a boundary layer of 8-10 nm has a Si-Ta composition as determined by EELS.

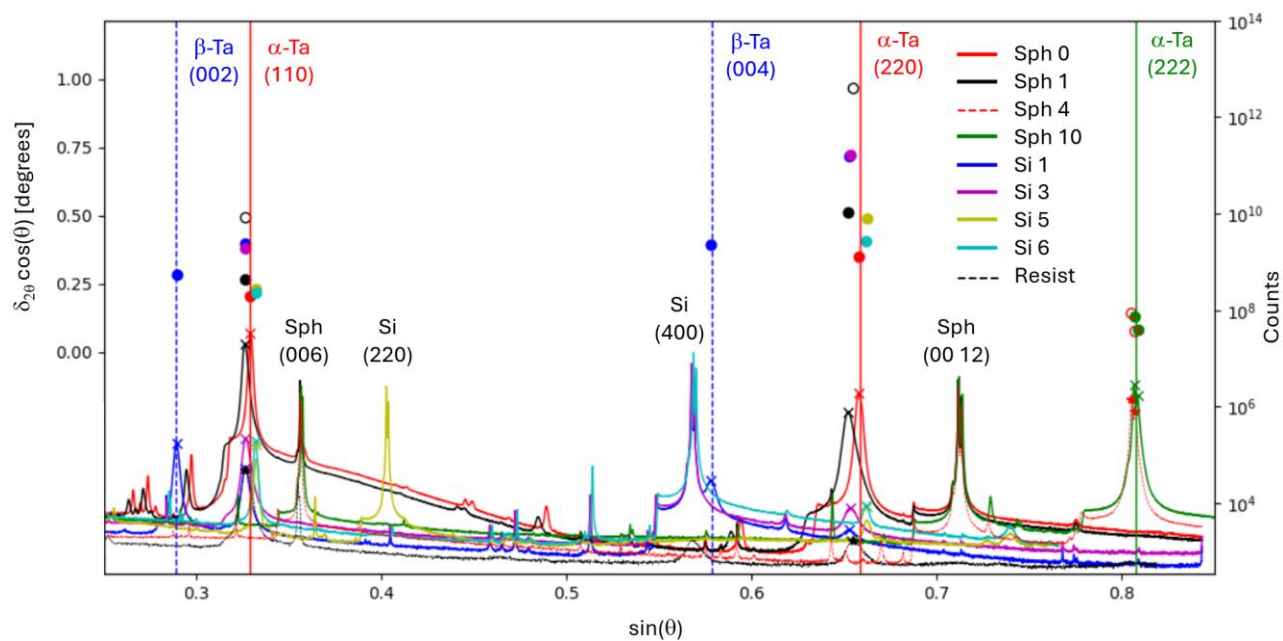


**Figure S2. Williamson-Hall plot of XRD data.** The full XRD spectra are plotted as a function of  $\sin(\theta)$ , emphasizing the relative contributions of strain and grain size broadening of the  $\alpha$ -Ta reflections. The circles represent the FWHM of the peaks, scaled by the cosine [ $\delta_{2\theta} \cos(\theta)$ ], and are plotted on the left hand axis. The (220) reflections are considerably broadened at the higher angle. By contrast, the (222) reflection of Sph 10 and Sph 4 remain sharp at the high angle where they occur.

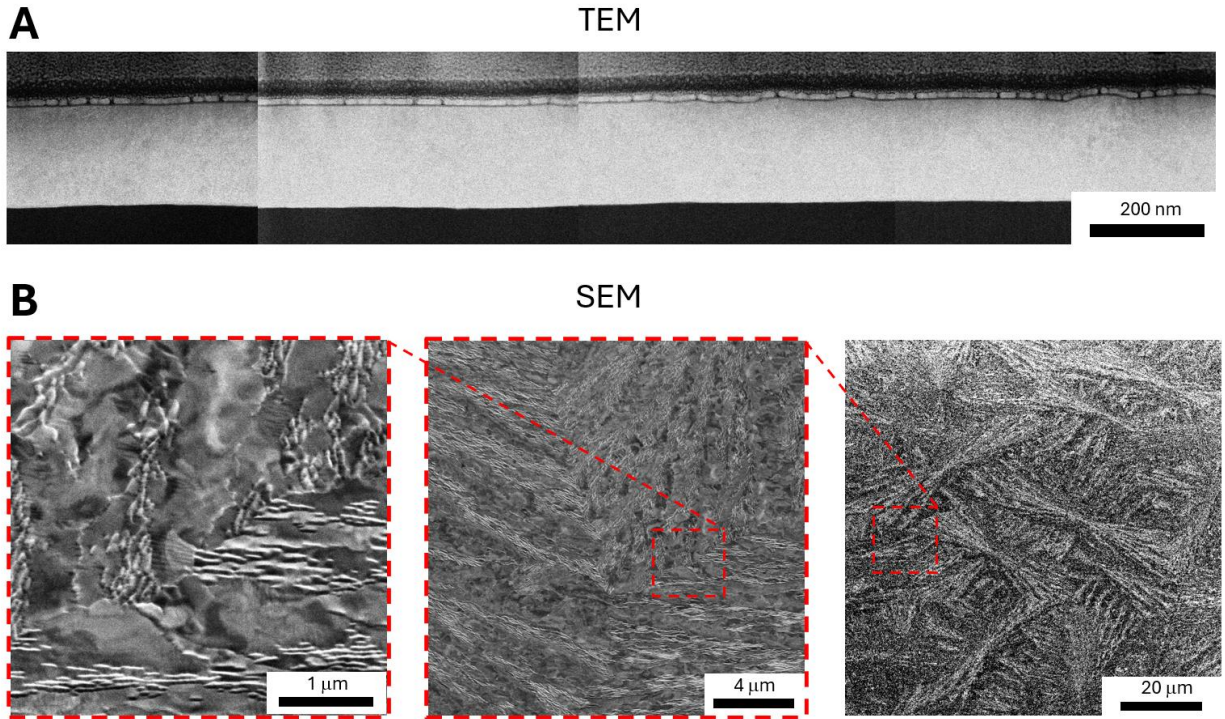


**Figure S3. Grain texturing of Ta on Si (Sample Si 6).** (A) Relatively smooth films grow on Si under the conditions described in the main text, as seen in the wide-field TEM image here. (B) Nonetheless the films Si 5 and Si 6 displayed distinctive texturing spanning a  $\sim 100$   $\mu\text{m}$  length scale. As can be seen in the SEM images, the dendritic structure consists of alternating bands of wide and narrow grains. The largest structures, as in the rightmost image, were very uniformly distributed over the wafer above this scale. The structure may originate in electric fields present in the films during growth.